NEAR GRAZING SCATTERING FROM NON-GAUSSIAN OCEAN SURFACES

Yunjin Kim and Ernesto Rodríguez
Jet Propulsion Laboratory
California Institute of Technology
4800 Oak Grove Dr.
Pasadena, CA 91109

Short Title: NEAR GRAZING OCEAN SCATTERING
(RADIO SCIENCE)

December 29, 1993

Abstract

In this paper, we investi gate the behavior of the scattered electrom agnetic waves from non-G aussian ocean surfaces at near grazing incidence. From the experimental ocean scattering data, it has been observed that the backscattering cross section of a horizontally polarized wave can be as large as the vertical counterpart at near grazing incidence. In addition, these returns are highly intermittent in time. Using numerical scat tering simulations, it can be shown that the horizontal average backs cattering cross section cannot be larger than the vertical counterpart for the Gaussian surfaces. Our main objective of this study is to gain a clear understanding of near-grazing scattering mechanisms and statistics from ocean surfaces which arc intrinsically non-Gaussian. For the ocean surface modeling, wc generate Gaussian surfaces from the ocean surface power spectrum which is derived using several experimental data. Then, nonlinear hydrody - namic characteristic is introduced using an efficient method. For surface scattering, we usc MOM (Method of Moments) to calculate the scattered fields from ocean patches. The differences between Gaussian and non-G aussian surface scattering at near grazing incidence arc presented. We also discuss the polarimetric dependence and statistics of the scattered fields from ocean surfaces.

1. INTRODUCTION

Scattering from an ocean surface at near gi azing incidence has been studied both theoreti - cally and experimentally by many resea rchers [See, for example, Lewis and Olin, 1 980; Wetzel, IWO; Trizna, 1991; Ri no and Ngo, 1993]. According to experimental observations, radar backscatter at grazing incidence angles shows an interesting polarization dependence which has not been explained satisfactorily using theoretical models. Specifically, the backscatter ratio $\frac{\sigma_{HH}}{\sigma_{VV}}$ comes closer to unity than predic ted by many thin-dim. High resolution radar returns show high intensity sea spikes which are inter mittent in time. For these sea spikes, σ_{HH} can be larger thau σ_{VV}. '1'here have been so me suggestions that these unexpected observations may come from shadowin g or feature scattering [Wetzel, 1990]. However, currently, there is no clear understanding of the origin of these phenomena. In order to discover their cause, one must model ocean surfaces realistically. Many canonical and and

semi-empirical features, such as cylinders, wedges, sharp crests, sloshes and plumes, have been used for this purpose [Wetzel, 1990]. In this paper, we perform a numerical experiment which includes nonlinear wave interactions derived from the law of hydrodynamics [Creamer et al., 1989] and calculate the scattered field using MOM (Method of Moments) to understand scattering behavior at grazing incidence.

As discussed in the previous paragraph, both hydrodynamic modeling of ocean surfaces and an accurate near grazing scattering theory are required in order to evaluate the scattered field from the ocean surfaces at near grazing incidence. For the surface modeling, we generate Gaussian surfaces from the ocean surface power spectrum derived using several experimental data [Rodriguez et al., 199'2]. Then, nonlinear effects are introduced using a new approach developed by Creamer et al [1 989]. For surface scattering, we implemente MOM to calculate the backscattering from ocean surface patches. Since 110 analytical scattering theories have been proven to be accurate for near grazing scattering, we implemented MOM even though full two dimensional ocean surfaces cannot be used. Even with MOM, it is well known that, if the conventional incident wave tapering [Thorsos, 1988] is used, the scattering patch length must be very large (usually much larger than 100 λ) for near grazing scattering. Here, λ is the wavelength of the incident electromagnetic wave. For incidence angles larger than 80 degrees, the scattering patch length requirement prevents us from using the tapered MOM (popularly known as the tapered integral equation method). Here, we use periodic boundary conditions and the periodic Green's function is accurately evaluated using the method suggested by Veysoglu et al. [1991] in order to avoid the unreasonably large patch lengths.

The purpose of this paper is to examine the effects of nonlinear ocean surfaces in order to determine the origin of the curious scattering phenomena at near grazing incidence. The statistics of near-grazing scattering are investigated and compared with the scattering statistics at modest incidence angles. Especially, the polarimetric dependence of near-grazing scattering is contrasted with that at modest incidence. However, we emphasize that the ocean surface modeling in this paper dots not include several important features present

in the real ocean. First, we ignore breaking waves since they are not well enough understood to be included in the hydrodynamic modeling. Second, we have neglected wind forcing which is of importance in determining the Inoculation and phase for very short waves. This may not affect significantly our evaluation of the scattering cross section since we consider the S-hand (λ =-15 cm) scattering. '1'bird, we assume perfectly conducting one-dimensional surfaces for computational simplicity. '] 'horsos [1990] has studied the scattering cross section for Gaussian ocean-like surfaces at 80 degrees incidence. Our approach differs from his in that we consider nonlinear ocean effects, polarization effects and smaller wavelengths and incidence angles.

The outline for this paper is the following. In the next section, we present a method to generate non-Gaussian ocean surfaces. The bistatic scattering cross sections are calculated in the third section. The fourth section presents the statistics of the backscattering cross section at near grazing incidence. The final section summarizes our conclusions.

2. Non Gaussian Ocean Surface Generation

In order to realistically model ocean surfaces, one must include the nonlinear hydrody - namic effects. This nonlinear interaction of ocean waves produces the Electromagnetic Bias effect when the ocean is illuminated from tile nadir direction [See, for example, Rodríguez et al., 1992]. However, non-Gaussian surface effects for near grazing scattering are not well understood. In this section, we present an existing technique to include the nonlinear interaction using a linear representation of ocean surface waves developed by Creamer et al []989]. To our knowledge, this method was first implemented for ocean scattering by Rino et al. [1991]. In the following paragraph, we summarize the method.

For one-dimensional surfaces, this method is particularly simple to implement. For detailed mathematical and physical explanation for arbitrary two-dimensional spectra, the reader is referred to the original paper [Creamer et al., 1989]. The recipe is as follows, First, generate a Gaussian surface from the proposed ocean spectrum $F(k)$ as

$$F(k) = k^{-2.5}[s_1 e^{-k/k_1} + s_2 e^{-k/k_2}] \qquad k > k_0 \tag{1}$$

$$k_0 = g/U^2 \tag{2}$$

$$k_1 = 2\pi/3 \quad [m^{-1}] \tag{3}$$

$$k_2 = 2\pi/0.02 \quad [m^{-1}] \tag{4}$$

where k is the wavenumber, g and U are the acceleration of gravity and the wind speed measured at 10 m, respectively. The spectral strengths s_1 and S_2 are chosen based 011 some experimental data and the details can be found in Rodríguez et al. [1 992]. Then, after removing the mean height of the Gaussian surface, take Hilbert transform $d(x)$ as

$$d(x) = \frac{1}{\pi} P \int \frac{h_G(x') - < h_G >}{x - x'} dx' \tag{5}$$

where $P \int$ is the principal value integral and h_G is a Gaussian surface height. Next, perform a coordinate transformation using

$$x' = x - d(x). \tag{6}$$

Finally, take an inverse Hilbert transform and add mean to generate non-Gaussian ocean surfaces given by

$$h_{NG}(x) = \frac{-1}{\pi} P \int \frac{d_c(x')}{x - x'} dx' + < h_G > \tag{i'}$$

where h_{NG} is a non-Gaussian surface and $d_c(x')$ is the coordinate transformed Hilbert transform.

If Gaussian and non-Gaussian surfaces are compared, they show significant differences even though their spectra are similar. The most relevant difference is that the small scale surface roughness is modulated by the large waves owing to nonlinear wave interactions. We have examined this using our surface height data to verify these nonlinear effects. Both Gaussian and non-Gaussian surfaces were divided into 4096 patches of 1 meter length. For each patch, we calculated the mean height, rms slope, and average radius of curvature. The average radius of curvature r_c is given by

$$r_c = \frac{1}{< | K(x) | >} \tag{8}$$

where

$$K(x) = \frac{h_{xx}(x)}{[1 + h_x^2(x)]^{3/2}} \tag{9}$$

and h_x and h_{xx} are the first and second derivatives of the surface height. 'J'hew? surface roughness parameters were binned according to their mean height. The results for 10 m/sec wind speed are shown in Fig. 1. As shown in Fig. 1, the surface roughness of non-Gaussian surface increases for larger mean height. This is evident from both rms slope and radius of curvature. This is expected results from nonlinear interaction of waves [Longuet-Higgins and Stewart, 1961].

3. Radar Cross Section Calculations

In this section, we calculate bistatic cross sections from simulated ocean surfaces using MOM. Even though MOM demands intensive numerical computation, we use it since 110 analytic techniques have proven accurate for near grazing scattering. In order to evaluate the scattering cross section from a large ocean surface, we divide the surface into many 80 wavelength patches and scattering from each patch is calculated using MOM. Notice that, each patch was tilted by the large waves. This tilting changes the local incidence angle and it also provides the shadowing due to large wave components. In our simulation, we used 324 patches of 12.5 meter and the incidence wavelength was 15.625 cm. The scattered fields from each patch were incoherently averaged to obtain the bistatic cross section.

The scattered field was computed using MOM assuming periodic boundary condition in order to reduce the edge current effect. Due to this periodic condition, we do not have to taper the incident field but we must evaluate the periodic Green's function which is an infinite summation. Hence, even though we remove the large patch length requirement of the tapered incident wave method at near grazing, the computational burden is on the evaluation of the periodic Green's function. Here, we converted the Green's function to an integral using a Laplace transform pair following the technique by Veysoglu et al. [1991]. The detailed implementations of this method are presented elsewhere [Rodriguez and Kim, 1993a].

The bistatic cross sections of both Gaussian and non-Gaussian surfaces are shown in Fig. 2 for three different incidence angles. For modest incidence angles (Fig 2(a) and (b)), we notice that there is almost no differences in the bistatic cross sections of Gaussian and non-Gaussian surfaces. For grazing incidence angle (Fig.2 (c)), the bistatic cross section of the non-Gaussian surface is higher than its Gaussian counterpart by 2 to 3 dB for H-polarization. However, for V-polarization, the non-Gaussian features make almost 110 differences in the bistatic cross section. This may suggest that if highly non-Gaussian sharp features are introduced, the H-polarization backscatter can be highly enhanced compared with the V-polarization case. From the Fig. 2(c), the difference between H- and V-polarization backscattering cross sections is 30 dB.

For near grazing scattering, it is important to consider shadowing effects which may be affected by 12.5 meter patch size. In order to examine the patch size effect, we increase the patch length to 25 meters and calculate the bistatic cross section. The results arc shown in Fig. 3. 'J'here is almost **no** difference between the bistatic cross sections of two patch lengths for either polarization. Even though this results cannot prove that the further increase in patch length will not affect the bistatic cross section, it is very suggestive that 12.5 meter pate.11 is long enough for the S-band scattering calculation.

4. Statistics of Backscattering Cross Section

The bistatic cross section shown in the previous section can be considered as the scattering response of a low resolution radar. For our numerical calculation, the radar footprint was 4 km. Since wc calculate the scattered field from each 12.5 meter patch, we can simulate the backscattered returns for a high resolution radar. The results are shown in Fig. 4. From Fig. 4, it can be noticed that stronger returns of σ_{HH} are more sporadic than those of σ_{VV}. Similar experimental observation was reported by Lewis and Olin [1 980] for sca spikes using 9.2 GHz pulses. However, the stronger returns in Fig. 4 c/o not appear to be sea spikes since tile vertical backscatters arc much stronger (approximately 30 dB) than the horizontal ones. Based on the observations by Lewis and Olin, the largest backscatter was due to whitecaps. Since whitecaps and breaking waves are not included in our modeling, the absence of sea

spikes in our simulation can be understood. Hence, to verify the experimental observations by Lewis and Olin, we must model the breaking events in our numerical simulation.

From the backscattering cross sections from 12.5 meter patches (Fig. 4), one can notice that H- and V- polarization cross sections vary differently. That is, V-polarization backscatter can be relatively small when H-polarization has a strong backscattering cross section and vice versa. In order to quantify this phenomenon, we calculated the correlation coefficient (γ_{HV}) of H- and V-polarization backscattering cross section defined as

$$\gamma_{HV} = \frac{< \sigma_{HH}\sigma_{VV} > - < \sigma_{HH} >< \sigma_{VV} >}{(< \sigma_{HH}^2 > - < \sigma_{HH} >^2)(< \sigma_{HH}^2 > - < \sigma_{HH} >^2)} \tag{10}$$

where $<>$ denotes the ensemble average. The H-V correlation coefficients for three incidence angles are shown in Fig. 5. For the nadir looking radar returns, σ_{HH} and σ_{VV} are perfectly correlated. As the incidence angle increases, they become decorrelated which suggests that the contributing scatterers of H- and V-polarized returns may be very different. This has been experimentally observed [Sletten et al., 1993]. The decorrelation due to the increase of the incidence angle may be an intrinsic characteristic of rough surface scattering because similar behavior can be observed for Gaussian surfaces [Rodríguez and Kim, 1993a]. One can also evaluate the correlation coefficient of the field quantities (E_{HH} and E_{VV}^*) in order to examine both amplitude and phase correlations. Here, E is the backscattered electric field and $*$ denotes the complex conjugate. Using the same data, it can be shown that both backscattered cross section and field show strong decorrelation for higher incidence angles.

We also examined the temporal variation of the backscattered field using the wavelet transformation and the results are presented elsewhere [Rodríguez and Kim, 1993b]. In order to study the temporal behavior, we calculated the backscattered fields from six patches of 12.5 meters for 10 seconds with 0.01 second sampling interval. Using these 6000 returns, we examined two interesting scattering mechanisms at near grazing incidence. They are tilt and hydrodynamic modulations. For the 85 degree incidence angle, we divided the backscattering cross section into several large wave tilt angles. The results are shown in Fig. 6. As expected, the backscattering cross section increases when the scattering patch is tilted toward the radar since the corresponding local incidence angle becomes smaller. For

the II-polarization case, 80 dB variation in the backscattering cross section can be observed while the V-polarization returns show 60 dB variation. One should remember that the tilt angle is strongly related to the patch size. Here, our scattering patch size is 12.5 meters. Another quantity that we considered is the hydrodynamic Inoculation. As shown in Fig. 1, we observed the increase of surface roughness for higher mean surface height. Hence, one can expect brighter returns from higher surface height for relatively large incidence angles. Unfortunately, we have to use long scattering patches (12.5 meters) for 85 degrees incidence angle. The largest ocean wavelength is 64 meters in our simulation. Due to the long patch length, the surface height resolution diminishes. Hence, we divided the backscattering cross sections into only three mean height bins as shown in Fig. 7. Clearly, for II-polarization, the hydrodynamic modulation is observed for Non-Gaussian surfaces. The hydrodynamic modulation for V-polarization is much smaller than the II-polarization case (not shown). More dramatic effects of the hydrodynamic modulation 011 the backscattered field can be seen from the temporal variation of the field [Rodríguez and Kim, 1993b].

If one considers the scatter-cd field from an ocean surface as the sum of many phasors from ocean scattering objects, the pdf (probability density function) of the field becomes Gaussian owing to the central limit theorem. The scattered field amplitude follows the Rayleigh distribution arid the corresponding intensity obeys the exponential distribution. If the backscattered cross section is normalized by its mean, the cdf (cumulative density function) of the normalized quantity becomes

$$CDF = 1 - e^{-p} \tag{11}$$

where

$$p = \frac{\sigma}{\langle \sigma \rangle} \tag{12}$$

When $log_e(1 - CDF)$ is plotted versus p, a line with the slope of -1 will be obtained if the scattered field follows the Gaussian statistics. We examined the calf's of the backscattering cross sections for three incidence angles. Three plots (cross: O, diamond: 45, and square:85 degrees incidence angles) are shown in Fig. 8 (a) and (b) for both Gaussian and non-Gaussian surfaces, respectively. As can be noticed from Fig. 8, both calf's show similar

behaviors. For O and 45 degrees incidence angles, it is evident that the scattered field satisfies the Gaussian statistics. However, the backscattered field for the 85 degree incidence angle is clearly non-Gaussian. The cdf of the near grazing scattering displays two distinct characteristics. One is a large number of low backscatter events due to shadowing. The other is the increase of the brighter returns which cause the long tail of the 85 degrees calf. It is interesting to notice that the II-polarization cdf has the longer tail than the V-polarization cdf for 85 degrees incidence angle. In addition, the non-Gaussian cdf (Fig. 8(b)) also shows the longer tail than the Gaussian counterpart. This departure from the Gaussian statistics has been experimentally observed by many researchers [See, for example, Wetzel, 1990; Trizna, 1 991].

5 Conclusions

We have examined the near grazing scattering cross sections from non-Gaussian ocean surfaces and their statistics. We simulated the non-linear hydrody namic interaction using a method by Creamer et al. [1989]. This simulated non-Gaussian ocean surface exhibits the increased surface roughness for higher mean surface height, as expected. The scattered field was evaluated using MOM with periodic bou ndary conditions. The periodic Green's function was efficiently calculated following a technique developed by Veysoglu et al. [1991].

When we compared the near grazing bistatic cross sections from Gaussian and non-Gaussian surfaces, only n-polarization case showed a noticeable difference. This implies that the II-polarization sea spikes may be originated from the sharp non-Gaussian featu res. From the simulation results, the 11-polarized backscattered field was found to be more sporadic than its V-polarized counterpart at near grazing incidence. As the incidence angle increases, the H- and V-polarized backscattered fields become deem-related, We also considered the cdf of the backscattering cross section and found that the backscattered field at modest incidence angles satisfied the Gaussian statistics while a remarkable deviation was observed from the near-grazing backscattered fields. The scattering mechanisms of the large backscatter variation at near grazing incidence may be due to shadowing and tilt and hydrodynamic modulations.

Our simulation showed that the S-band H-polarization backscattering cross section at 85 degrees incidence angle was lower than the V-polarization counterpart by 28 dB. This difference is not in agreement with the experimental observations. We could not find the H-polarized sea spikes which might be larger than the V-polarized sea spikes. These disagreements may come from the absence of breaking waves and sharp scattering features in our simulation. The perfectly conducting surface assumption may have profound effects on the near grazing sea spikes [Rino, personal communication]. The inclusion of the above-mentioned factors in our scattering simulation is under current consideration.

ACKNOWLEDGEMENTS

The research described in this paper was carried out by the Jet l'repulsion laboratory, California Institute of Technology, and was sponsored by the Office of Naval Research.

REFERENCES

Creamer D. B., F. Henyey, R. Schult, and J. Wright, Improved linear representation o f ocean surface waves, J. Fluid Mech., 205, 135-161, 1989.

Lewis B. 1,. and 1. D. Olin, Experimental study and theoretical model of high-resolution radar backscatter from the sea, Radio Sci., 15(4), 815-828, 1980.

Longuet-Higgins M. S. and R. W. Stewart, The changes in amplitude of short gravity waves 011 steady, non-uniform currents, J. Fluid Mech., 10, 529-549, 1961.

Rino C. 1,., 'J'. 1,. Crystal, A. K. Koide, H. D. Ngo, and 11. Guthart, Numerical simulation of backscatter from linear and nonlinear ocean surface realizations, Radio Sci., 26(1), 51-71, 1991.

Rino C. 1,. and 11. 1). Ngo, The application of beam simulation to scattering at low grazing angles part 11: occml-like surfaces, submitted to Radio Sci.

Rodríguez E., Y. Kim, and J. M, Martin, The effect of small-wave modulation on electromagnetic bias, J. Geophys. Res. 97 (C2), 2379-2389, 1992.

Rodríguez E. ancl Y. Kim, Near Grazing Scattering from Gaussian Rough Surfaces: Numerical Results, submitted to Radio Sci., 1993a.

Rodríguez E. and Y. Kim, Wavelet analysis of scattering from moving ocean surfaces, submitted to Radio Sci., 1993b.

Sletten M. A., D. B. Trizna and J. WU, Ultra-wideband, polarimetric radar studies of breaking waves, Proceedings of PIERS, 96, 1993.

'1'1101s0s, E. 1., The validity of the Kirchhoff approximation for rough surface scattering using a gaussian roughness spectrum, J. Acoust. Sot. Am., 83(l), 78-83, 1988.

Thorsos, E. 1., Acoustic scattering from a "Pierson-Moskowitz" sea surface, J. Acoust. Sot. Am., 88(1 ,335-349,1990.

Trizna D. B., Statistics of low grazing angle radar sea scatter for moderate and fully developed ocean waves, IEEE Trans. Antennas Propag., AP-39, 1681-1690, 1991.

Veysoglu M. E., H. A. Yueh, R. T. Shin, and J. A. Kong, Polarimetric passive remote sensing of periodic surfaces, J. Electro. Waves Applic., Vol. 5, No. 3, 267-280, 1991,

Wetzel L. 11., Electromagnetic scattering from the sea at low grazing angles, in Surface Waves and Fluxes, Vol. 11, G. 1,. Geernaert and W. J. Plant (eds.), Kluwer Academic Publishers, Dordrecht, 1990.

FIGURE CAPTIONS

Figure 1: The relationship between surface roughness ((a) RMS slope, (b) radius of curvature) and the surface mean height due to the hydrodynamic modulation, Notice the increase of surface roughness for higher mean height for non-Gaussian surfaces.

Figure 2: 11- and V-polarization bistatic cross sections for (a) O, (b) 45 and (c) 85 degrees incidence angles. Both non-Gaussian (solid line) and Gaussian (dashed line) surface are considered.

Figure 3: 11- and V- polarization bistatic cross sections using 12.5 meters (solid line) and 25 meters (dashed line) scattering patches.

Figure 4: Radar (backscattering) cross sections from 324 non-Gaussian surface patches.

Figure 5: II-V correlation coefficients for three incidence angles.

Figure 6: Tilt modulations at 85 degrees incidence angle for (a) 11- and (b) V- polarizations.

Figure 7: II-polarization hydrodynamic modulation at 85 degrees incidence angle.

Figure 8: 11- aud V- polarization cumulative density functions of three incidence angles (cross: O, diamond: 45, and square: 85 degrees) for (a) Gaussian and (b) non-Gaussian surfaces.

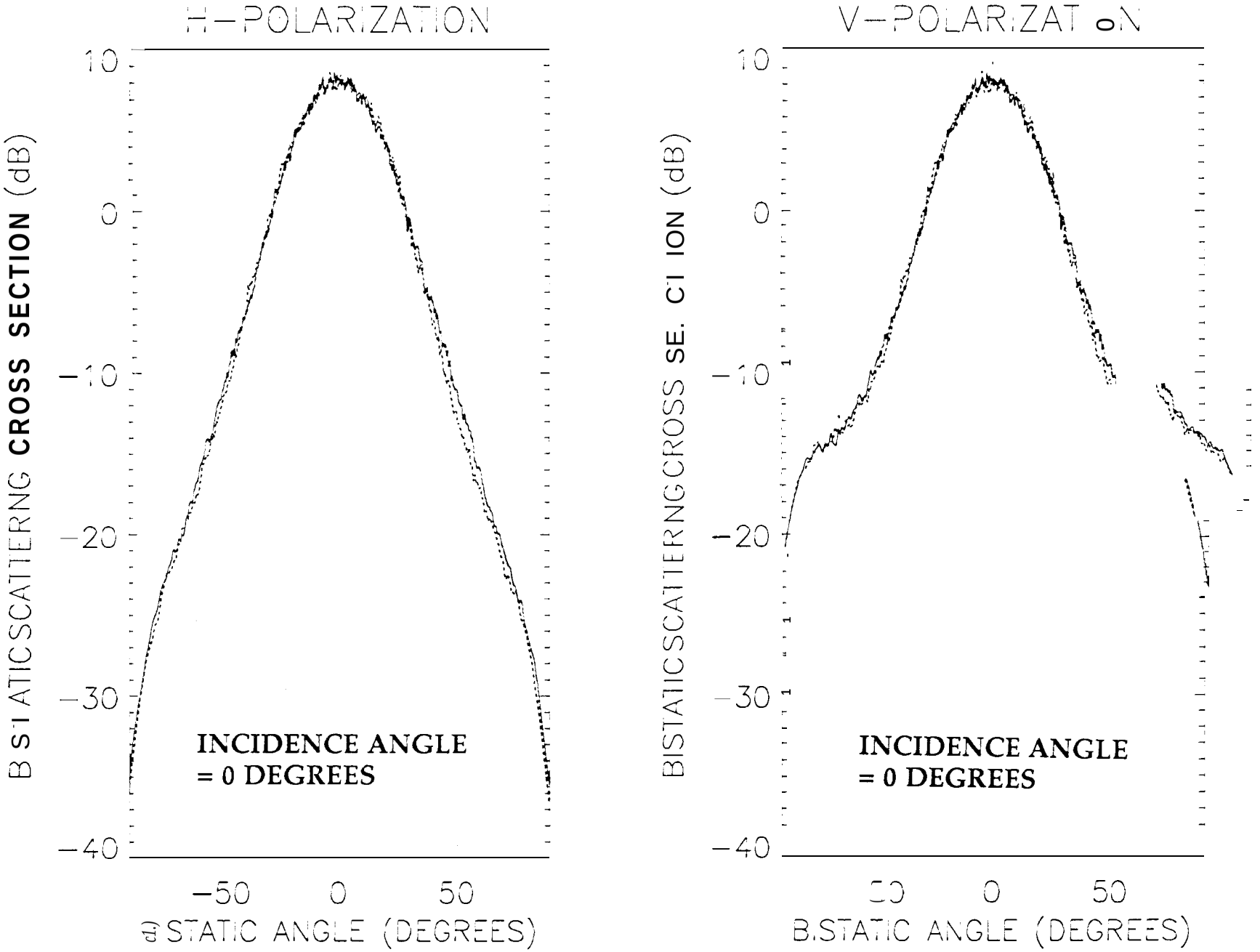
H—POLARIZATION
V—POLARIZATION
BISTATIC SCATTERING CROSS SECTION (dB)
10
0
−10
−20
−30
−40
INCIDENCE ANGLE
= 0 DEGREES
−50
0
50
BISTATIC ANGLE (DEGREES)

Fig. 2(a)

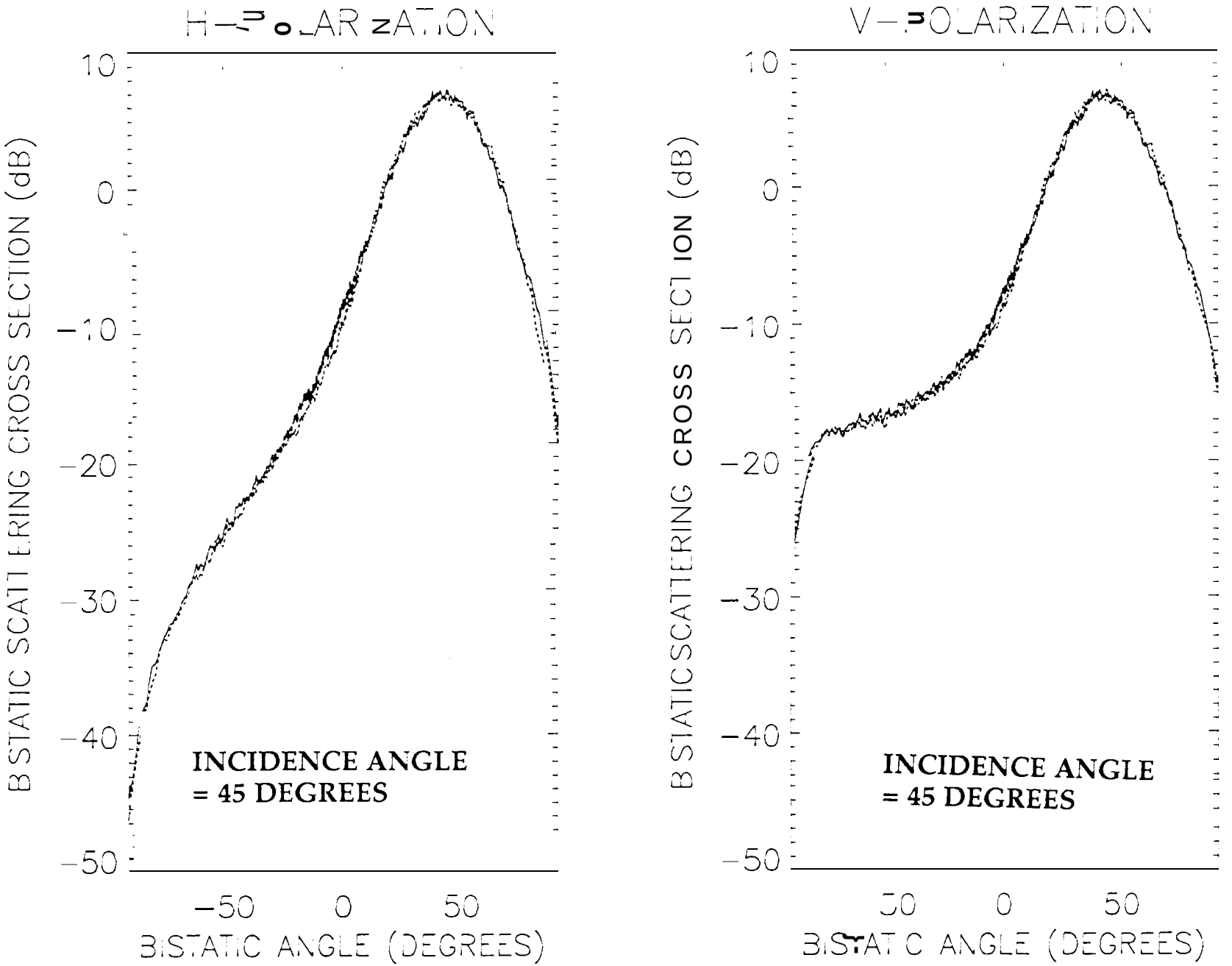
H-POLARIZATION
V-POLARIZATION
BISTATIC SCATTERING CROSS SECTION (dB)
10
0
-10
-20
-30
-40
-50
INCIDENCE ANGLE
= 45 DEGREES
-50
0
50
BISTATIC ANGLE (DEGREES)

Fig. 2(b)

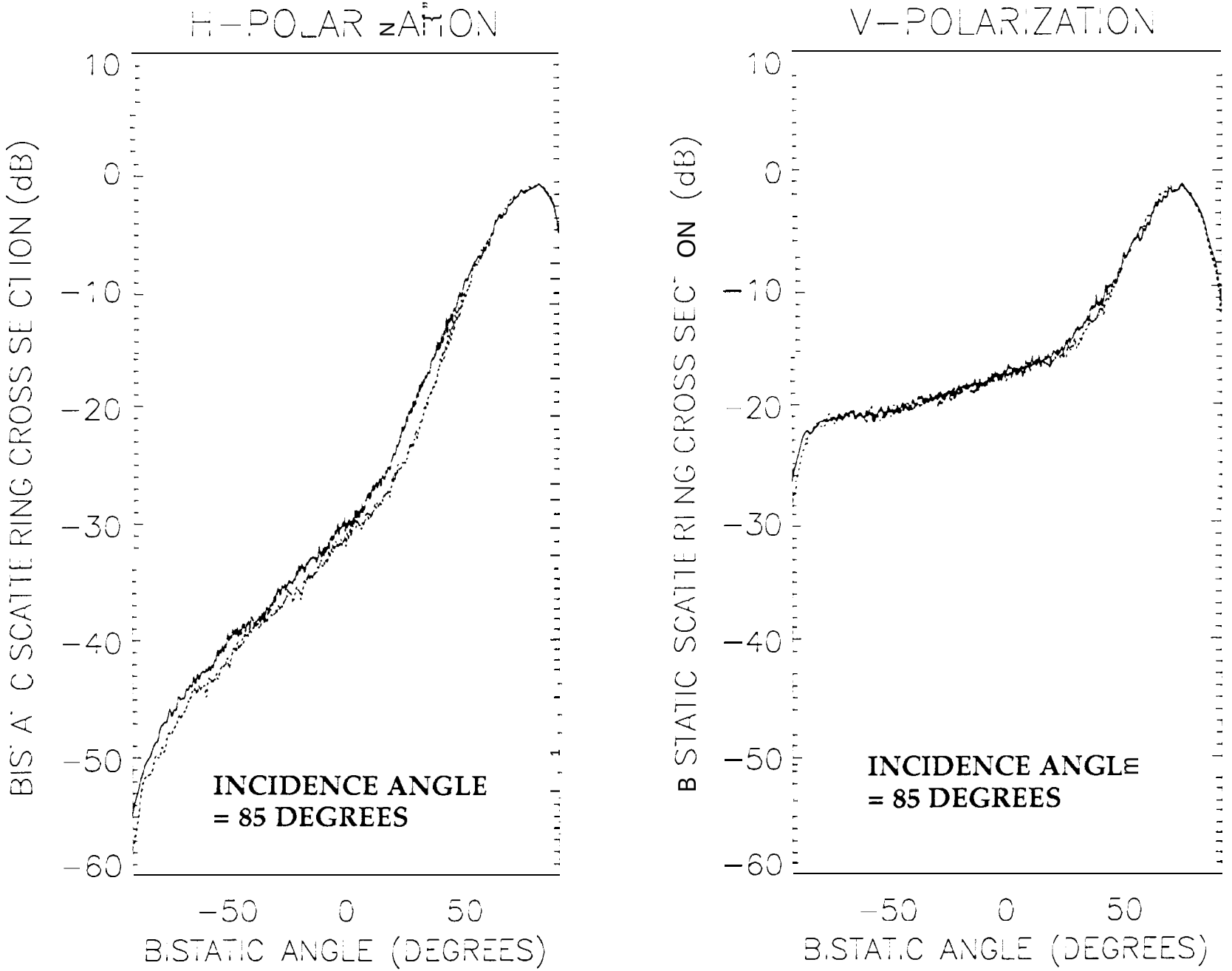
H—POLARIZATION
V—POLARIZATION
BISTATIC SCATTERING CROSS SECTION (dB)
BISTATIC SCATTERING CROSS SECTION (dB)
10
0
−10
−20
−30
−40
−50
−60
−50
0
50
BISTATIC ANGLE (DEGREES)
BISTATIC ANGLE (DEGREES)
INCIDENCE ANGLE
= 85 DEGREES
INCIDENCE ANGLE
= 85 DEGREES

Fig. 2(c)

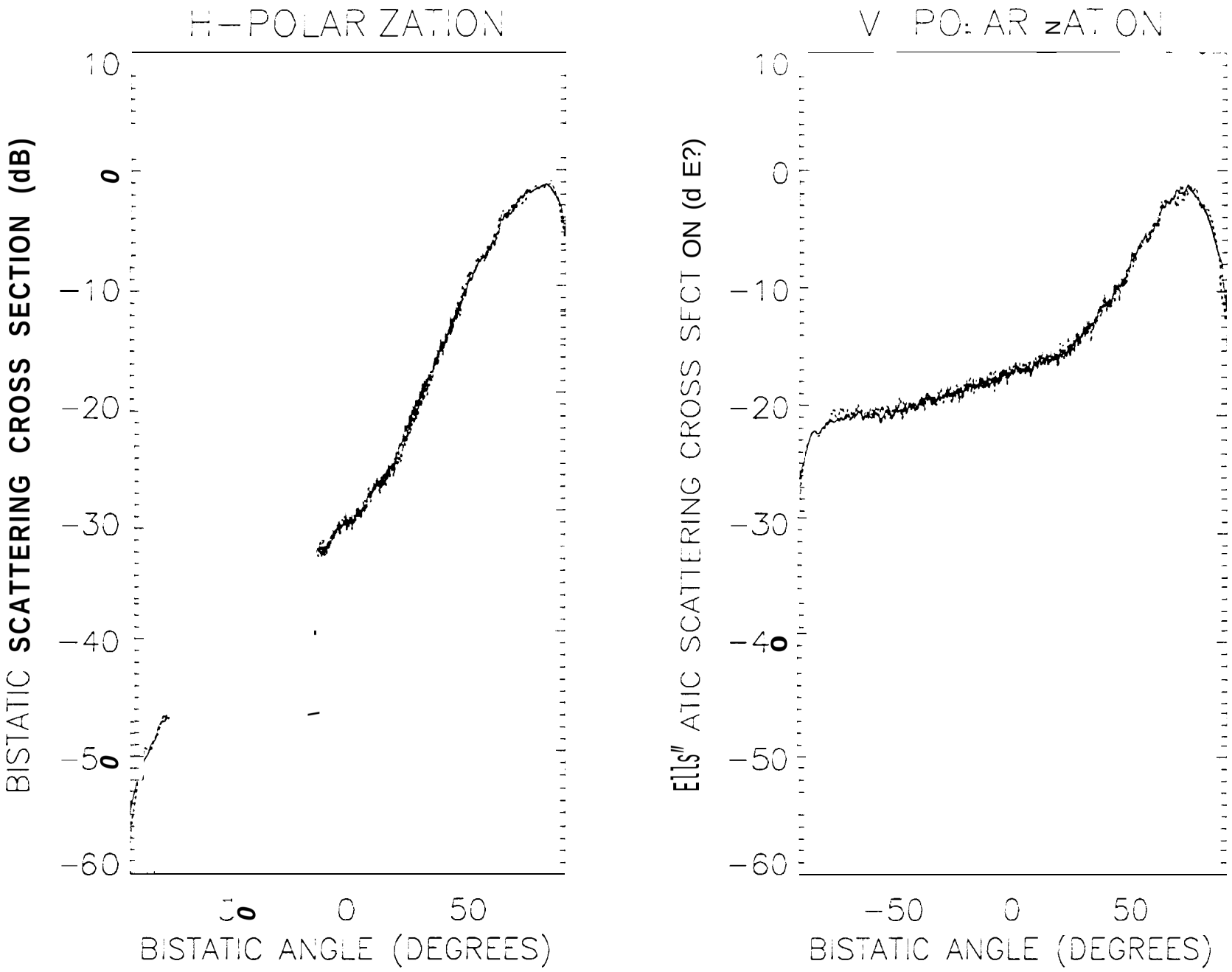
H—POLAR ZATION
BISTATIC SCATTERING CROSS SECTION (dB)
10
0
−10
−20
−30
−40
−5
−60
0
50
BISTATIC ANGLE (DEGREES)
V PO: AR zAT ON
Ells" AIIC SCATTERING CROSS SFCT ON (d E?)
10
0
−10
−20
−30
−4
−50
−60
−50
0
50
BISTATIC ANGLE (DEGREES)

Fig. 3

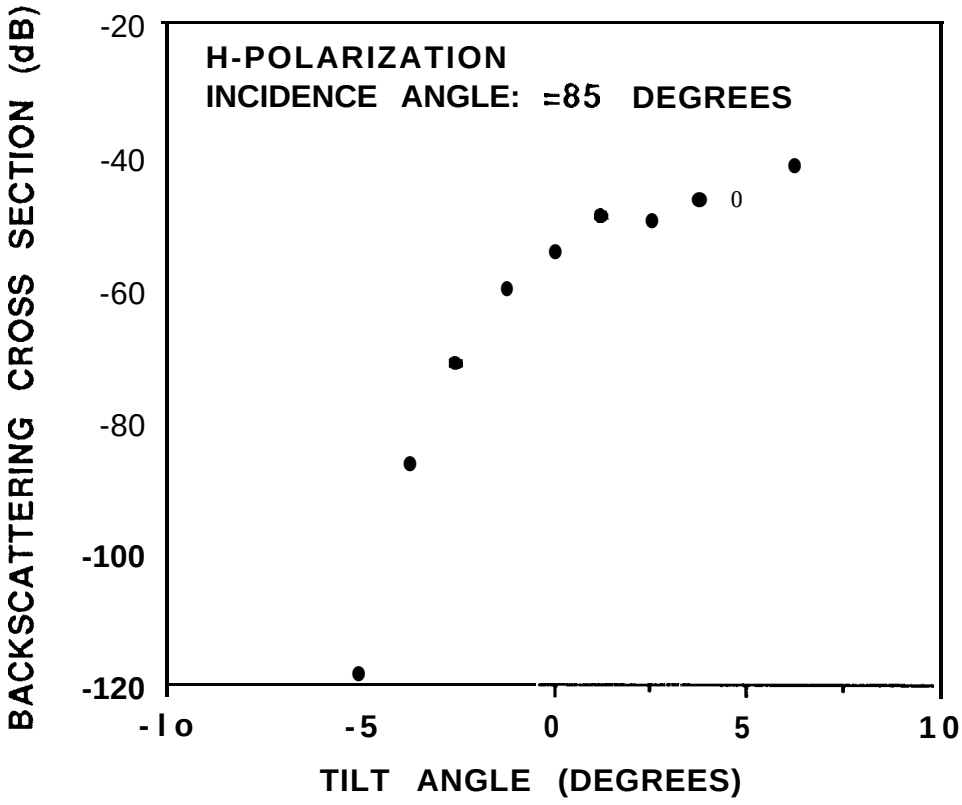
H-POLARIZATION
INCIDENCE ANGLE: =85 DEGREES
BACKSCATTERING CROSS SECTION (dB)
-20
-40
-60
-80
-100
-120
-lo
-5
0
5
10
TILT ANGLE (DEGREES)

Fig. 6(a)

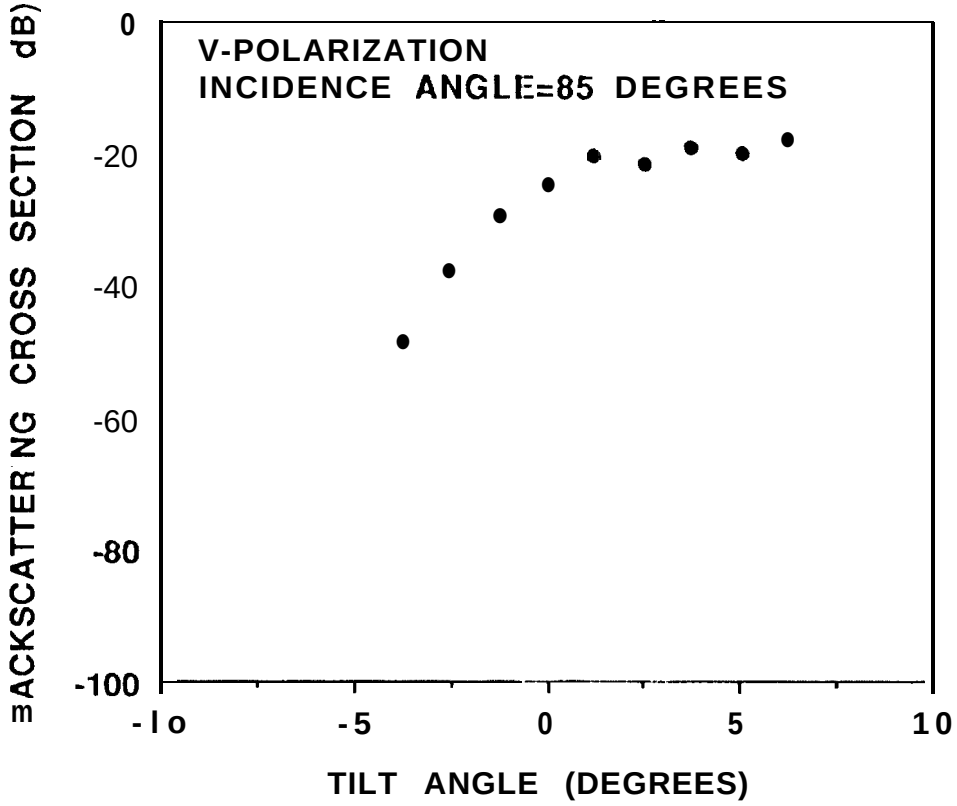
V-POLARIZATION
INCIDENCE ANGLE=85 DEGREES
BACKSCATTERING CROSS SECTION dB)
0
-20
-40
-60
-80
-100
-lo
-5
0
5
10
TILT ANGLE (DEGREES)

Fig. 6(b)

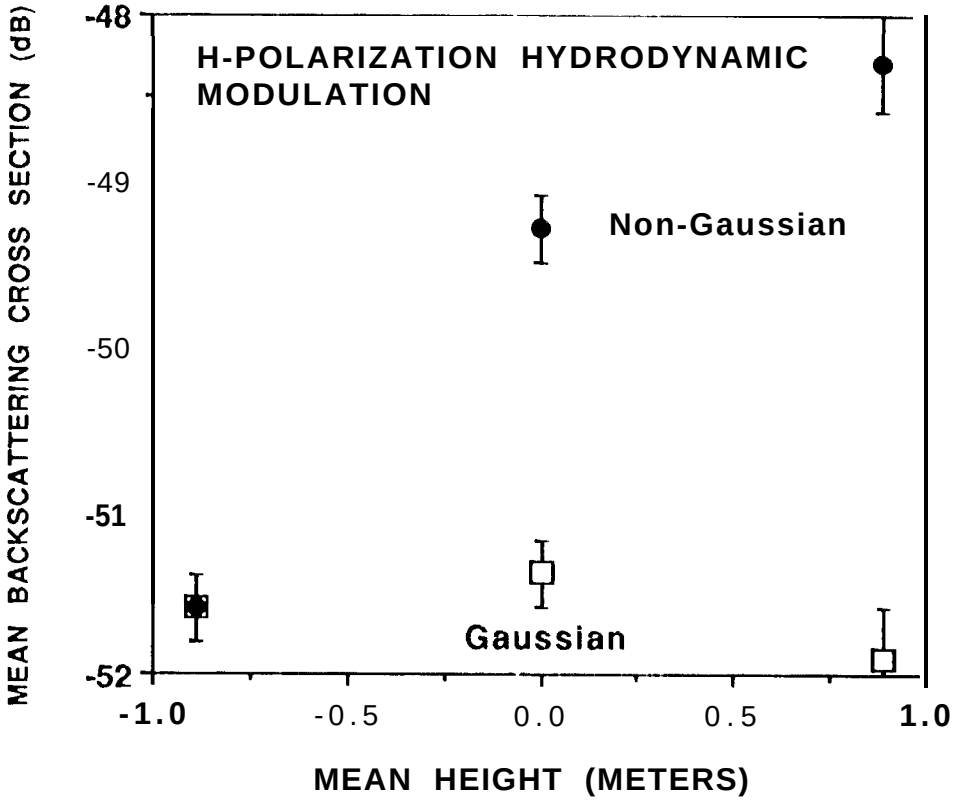
H-POLARIZATION HYDRODYNAMIC MODULATION
Non-Gaussian
Gaussian
MEAN BACKSCATTERING CROSS SECTION (dB)
-48
-49
-50
-51
-52
-1.0
-0.5
0.0
0.5
1.0
MEAN HEIGHT (METERS)

Fig. 7

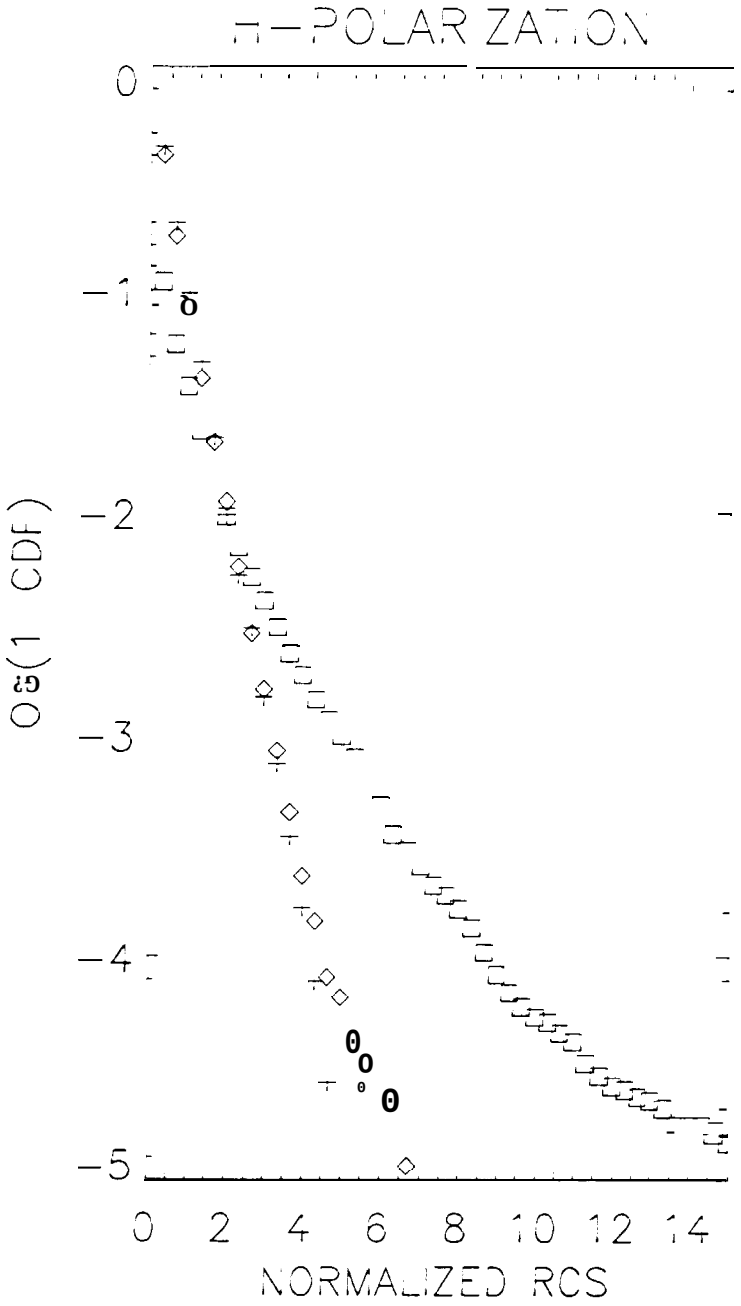
H—POLARIZATION
0
−1
−2
−3
−4
−5
0 2 4 6 8 10 12 14
NORMALIZED RCS

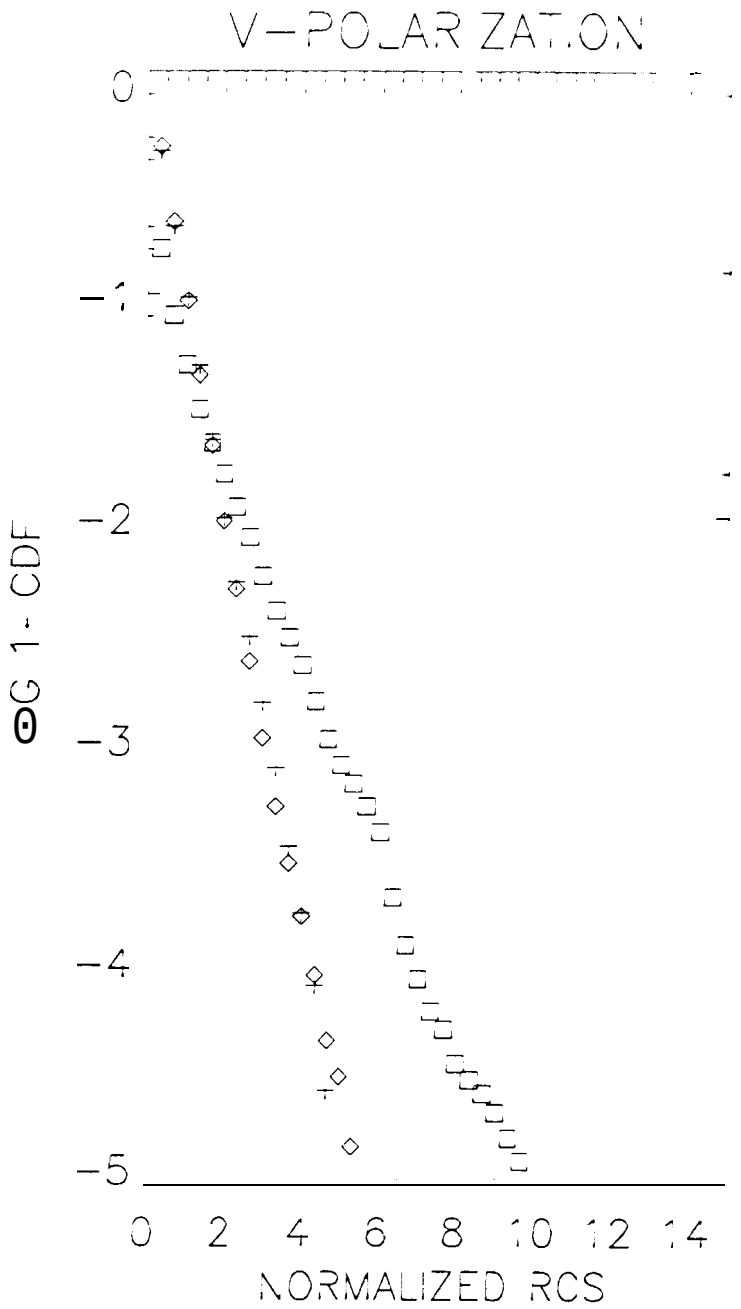
V—POLARIZATION
0
−1
−2
−3
−4
−5
0 2 4 6 8 10 12 14
NORMALIZED RCS

Fig. 8(a)

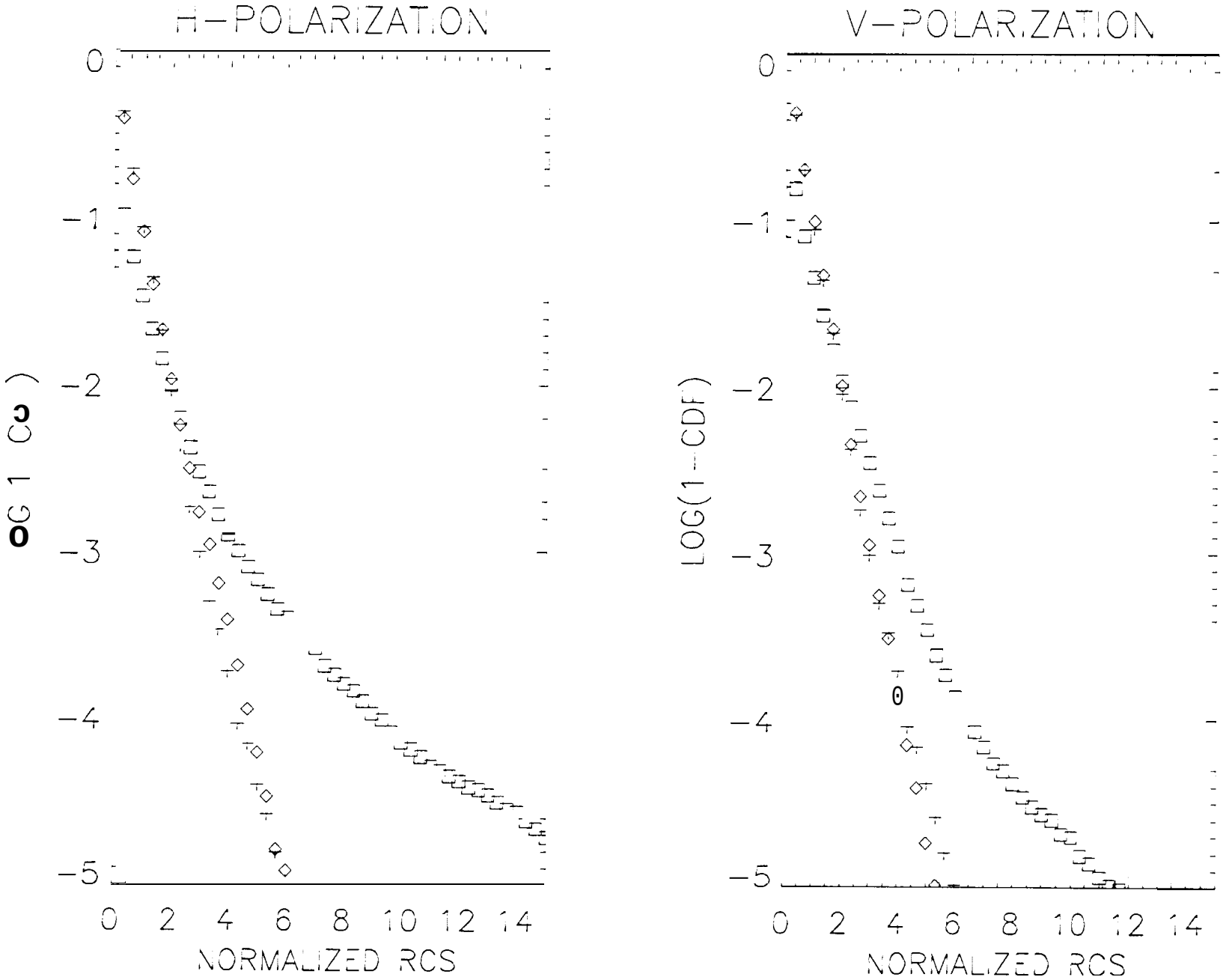
H-POLARIZATION
V-POLARIZATION
LOG(1-CDF)
NORMALIZED RCS
0
-1
-2
-3
-4
-5
0 2 4 6 8 10 12 14

Fig. 8(b)